

Supplementary information for

**Directed Dielectrophoretic Assembly and Separation on Microelectrodes
Patterned via Stereolithography 3D-Printed Shadow Masks**

Eunhwa Jo^{1,†}, Chanwook Cha^{1,†}, Yeongjun Kim², Jeongjae Seo², Eun Jung Lee^{1,2}, Koohee Han^{1,2,*}

¹School of Chemical Engineering and Applied Chemistry, Kyungpook National University, Daegu 41566, Republic of Korea.

²Department of Chemical Engineering, Kyungpook National University, Daegu 41566, Republic of Korea.

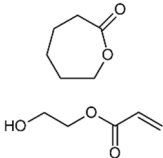
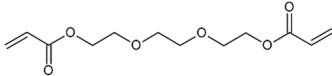
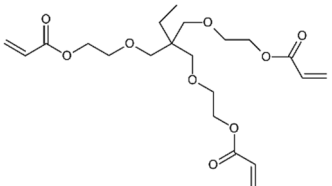
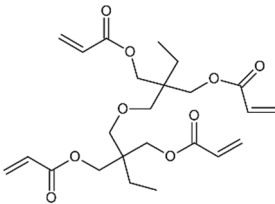
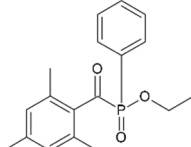
[†]Contributed equally to this work

*Corresponding author

Chemical composition of SLA resin

The chemical composition of the photocurable resin used for SLA printing is summarized in **Table S1**. The resin consists of one oligomer and three acrylate-based monomers with varying functionalities, along with a photoinitiator. The oligomer, 2-oxepanone homopolymer acrylate, serves as the base matrix providing flexibility and toughness. The monomers—including triethylene glycol diacrylate, ethoxylated trimethylolpropane triacrylate, and a multifunctional diacrylate—act as crosslinking agents that control viscosity, curing rate, and mechanical strength. Ethyl phenyl(2,4,6-trimethylbenzoyl)phosphinate is added as a photoinitiator to trigger polymerization under UV exposure.

Table 1. Composition of the UV-sensitive resin (Anicubic) used for SLA printing

Substance	Function	Percentage (%)	Structure
2-Oxepanone, homopolymer, 2-[(1-oxo-2-propenyl)oxy]ethyl ester	Oligomer	40-50	
2,2'-(ethylenedioxy)diethyl diacrylate; triethylene glycol diacrylate	Monomer	20-30	
Propylidynetrimethanol, ethoxylated, esters with acrylic acid	Monomer	10-25	
2-[[[2,2-bis[[[(1-oxoallyl)oxy]methyl]butoxy]methyl]2-ethyl-1,3-propanediyl diacrylate	Monomer	5-20	
ethyl phenyl(2,4,6-trimethylbenzoyl)phosphinate	Photoinitiator	1-3	

SLA 3D printing process for shadow masks

Shadow masks with various electrode geometries—including (a) staggered castellated, (b) triangular-tipped/flat-edge, (c, d) opposing sharp-tipped, and (e) square-island arrays—were fabricated using an SLA 3D-printing process. **Table S2** summarizes the overall dimensions and printing time of the shadow mask designs. Prior to printing, each 3D model was converted into the proprietary sliced format required by the SLA printer.

Since the total printing time in SLA systems is determined by the z-axis length, and all designs were printed at the same orientation, their printing times are similar. This time is highly dependent on a key parameter, the tilt angle. Printing them at 0° (parallel to the build plate) is fast (18 mins), but the large surface contact area causes significant surface tension, often resulting in print failure. Tilting the structure reduces this surface tension but takes longer due to the increased z-axis length (e.g., 52 mins at 30° and 65 mins at 45°).

Under our printing conditions, a minimum reliable tilt angle of 30° was identified and selected as the optimal balance between print reliability, pattern fidelity, and processing efficiency.

Table S2. Printing conditions for shadow masks

Design		a	b	c	d	e
SLA printer		Photon M3 Premium, Anycubic				
Resin		UV-sensitive resin, basic (Anycubic)				
Dimension (L × W × H, mm)		28 × 15 × 2	28 × 15 × 2	28 × 15 × 2	28 × 15 × 2	28 × 22 × 2
Total printing time	0° tilt	19 mins				
	30° tilt	52 mins				
	45° tilt	65 mins				

Step-by-step workflow for patterned electrode fabrication using SLA-printed shadow masks

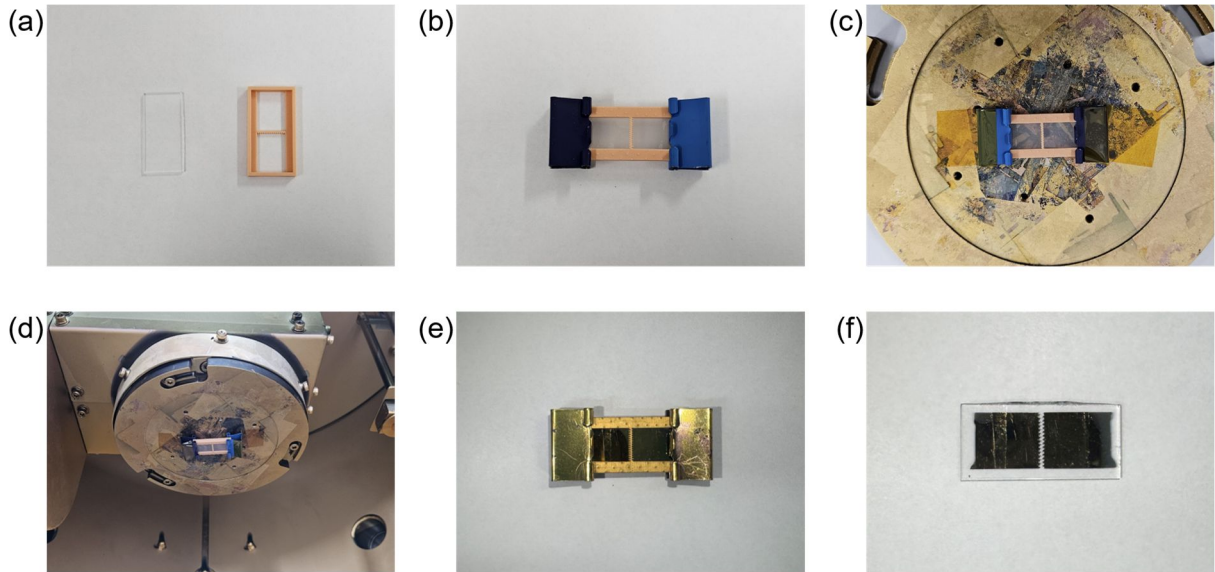


Figure S1. Fabrication workflow for electrodes utilizing SLA 3D-printed shadow masks and e-beam evaporation.

Figure S1 shows photographs of the fabrication process for patterned electrodes, achieved through selective e-beam evaporation using SLA 3D-printed shadow masks. The slide glass was cut using a diamond glass cutter. The cut glass was then sequentially bath-sonicated in acetone, ethanol, and deionized water for 5 minutes each (**Fig. S1a**). The slide glass was fitted inside the shadow mask to form an assembly. To ensure intimate contact, this assembly and a silicone pad were secured together using a binder clip (**Fig. S1b**). This assembly was then attached to an e-beam evaporator substrate using polyimide tape, with the shadow mask facing outward (**Fig. S1c**). The substrate was loaded into the vacuum chamber for metal deposition (**Fig. S1d**). During deposition, the entire surface, including both the shadow mask and the slide glass, was coated with metal (**Fig. S1e**). However, the shadow mask simultaneously prevented deposition onto the desired regions, resulting in the intended electrode pattern on the glass (**Fig. S1f**).

Comparison of 3D printing techniques

There are various types of 3D printing techniques, among which two-photon polymerization (2PP), fused deposition modeling (FDM), and stereolithography apparatus (SLA) are the most widely used. **Table S3** compares their key characteristics. 2PP operates by using the simultaneous absorption of two photons by a photosensitive material, which induces localized polymerization only at the laser focal point, thereby achieving extremely high spatial resolution beyond the diffraction limit. However, it has several limitations, including complex processing steps, high initial and maintenance costs, and a restricted output size. In contrast, FDM involves heating and extruding thermoplastic polymers, which makes the process relatively simple with low initial and maintenance costs. However, it offers a low resolution of several hundred micrometers. Lastly, SLA 3D printing works by using a UV exposure light to selectively cure and solidify layers of liquid photopolymer resin, building objects layer by layer with high precision. This method allows for the production of objects with higher resolution than FDM 3D printing at a comparable cost, while being simpler and more versatile than the 2PP method. Therefore, we used SLA 3D printing to fabricate precise, simply patterned masks at the lab scale for electrode patterning.

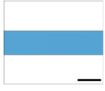

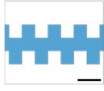
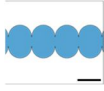



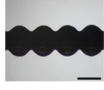

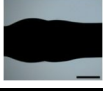


Table S3. Comparison of 2PP, FDM, and SLA methods

	2PP ¹	FDM ²	SLA ³
Manufacturing process	Additive manufacturing of two-photon polymerized photoresponsive materials ⁴	Additive manufacturing of thermoplastic materials	Stereolithography and additive manufacturing of photopolymerization ⁵
Process complexity	High	Low	Medium
Time	Long	Short	Medium
Initial investment cost	Very high (around \$500,000+)	Low (around \$1,000)	Low (around \$1,000)
Resolution	High (a few hundred nanometers)	Low (a few hundred micrometers)	Medium (tens of micrometers)
Output size	Very small to small	Medium to big	Small to big
Post-processing	Removal of residual strings, washing with isopropyl alcohol (IPA) followed by UV curing	Removal of residual strings and support structures	Removal of support structures, washing with isopropyl alcohol (IPA) followed by UV curing
Advantages	High resolution	Easy and rapid fabrication	Medium resolution, high surface quality, material versatility
Disadvantages	Very high cost, limited output size, complex process, residual waste	Low resolution, low surface quality	Odor emissions, residual waste

Comparison of geometric fidelity between FDM- and SLA-printed shadow masks

Table S4 displays the original CAD designs alongside the corresponding FDM- and SLA-printed shadow masks, while **Figure S2** presents the quantitative comparison of their geometric fidelity. For this analysis, optical microscope images were binarized and aligned with the CAD designs using ImageJ (National Institutes of Health, Bethesda, MD, USA). An XOR operation was then applied to quantify the deviation area (A_{diff}) between the printed pattern area and the original CAD design area (A_{CAD}). Geometric fidelity was calculated using the formula: $(A_{CAD} - A_{diff}) / A_{CAD}$. Both methods demonstrate high fidelity for (a) simple line structures (**Table S4a**). However, for complex nonlinear patterns—such as (b) triangular-tipped, (c) staggered castellated, and (d) sharp-tipped geometries (**Table S4b–d**)—FDM shows significant degradation due to nozzle diameter limitations and thermal shrinkage. In contrast, SLA printing utilizes non-thermal UV photopolymerization, which minimizes residual artifacts and eliminates thermal deformation. Consequently, SLA successfully reproduces fine, angular features with effective resolutions down to 50-200 μm , maintaining high geometric fidelity across all complex designs.

Table S4. Comparison of mask results by FDM and SLA 3D printing methods (scale bars = 500 μm)

	a	b	c	d
CAD design				
SLA				
FDM				

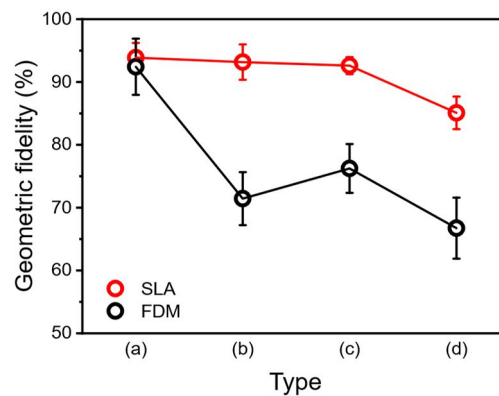


Figure S2. Comparison graph of geometric fidelity for shadow masks fabricated by FDM and SLA 3D printing methods, calculated relative to the original CAD designs.

Calculation of cross-over frequency for dielectrophoretic separation

The dielectrophoretic force exerted on a particle in an electric field is governed by

$$F_{DEP} = 2\pi\epsilon_m r^3 K \nabla E^2 \quad (1)$$

where ϵ_m is the permittivity of the medium, r is the particle radius, K is the Clausius-Mossotti (CM) factor, and ∇E^2 is the gradient of squared field magnitude. The sign of K determines the direction of motion: $K > 0$ for positive DEP (pDEP) and $K < 0$ for negative DEP (nDEP).

Under direct current (DC) fields, the CM factor is

$$K_{DC} = \frac{\epsilon_p - \epsilon_m}{\epsilon_p + 2\epsilon_m} \quad (2)$$

while for alternating current (AC) fields, the CM factor becomes complex:

$$K_{AC} = \frac{\epsilon_p - \epsilon_m - i(\sigma_p - \sigma_m)/\omega}{\epsilon_p + 2\epsilon_m - i(\sigma_p + 2\sigma_m)/\omega} \quad (3)$$

where ϵ_p is the permittivity of the particle, σ_p and σ_m are conductivities of the particle and the medium, and ω is the angular frequency. Only the real part of K_{AC} determines its sign:

$$\text{Re}(K_{AC}) = \frac{\epsilon_p - \epsilon_m}{\epsilon_p + 2\epsilon_m} + \frac{3(\epsilon_m \sigma_p - \epsilon_p \sigma_m)}{\tau_{MW}(\sigma_p + 2\sigma_m)^2 (1 + \omega^2 \tau_{MW}^2)} \quad (4)$$

Here, τ_{MW} is the Maxwell-Wagner charge relaxation time, defined as

$$\tau_{MW} = \frac{\epsilon_p + 2\epsilon_m}{\sigma_p + 2\sigma_m} \quad (5)$$

When the surface conductivity of the electric double layer (EDL) is significant, the particle behaves as if it has an additional surface conductance. In such cases, the particle conductivity is corrected as

$$\sigma_p = \sigma_{p,\text{base}} + \frac{2K_s}{r} \quad (6)$$

where K_s is the surface conductance of the particle.^{6,7}

The cross-over frequency is defined as the frequency at which $\text{Re}(K_{AC}) = 0$. Below this frequency, $\text{Re}(K_{AC}) > 0$ and the particle exhibits pDEP, whereas above this frequency, $\text{Re}(K_{AC}) < 0$ and the particle exhibits nDEP.

Geometric dimensions of patterned electrodes

Figure S3 shows schematic illustrations of the electrode patterned using an SLA 3D-printed mask. In the staggered castellated electrodes (**Fig. S3a**), the protruding rectangular segments have both a width and length of 300 μm , and the distance between the outermost tips of the opposing electrodes is also 300 μm . An asymmetric electrode configuration consists of triangular features on the top electrode and a straight-edged bottom electrode (**Fig. S3b**). The distance from the tip of the pointed electrode to the opposing straight electrode is 500 μm , while the distance from the indented region between the pointed electrodes to the straight electrode is 750 μm . The horizontal distance between adjacent tips is 600 μm . In the electrode configuration in which sharp tips face each other (**Fig. S3c and d**), the distance between adjacent tips is 500 μm , while the distances between opposing tips are 1000 μm (**Fig. S3c**) and 200 μm (**Fig. S3d**), respectively. In the diamond-island-shaped electrode, the diagonal length of each diamond island is 1000 μm , and the distance between adjacent islands is 200 μm (**Fig. S3e**).

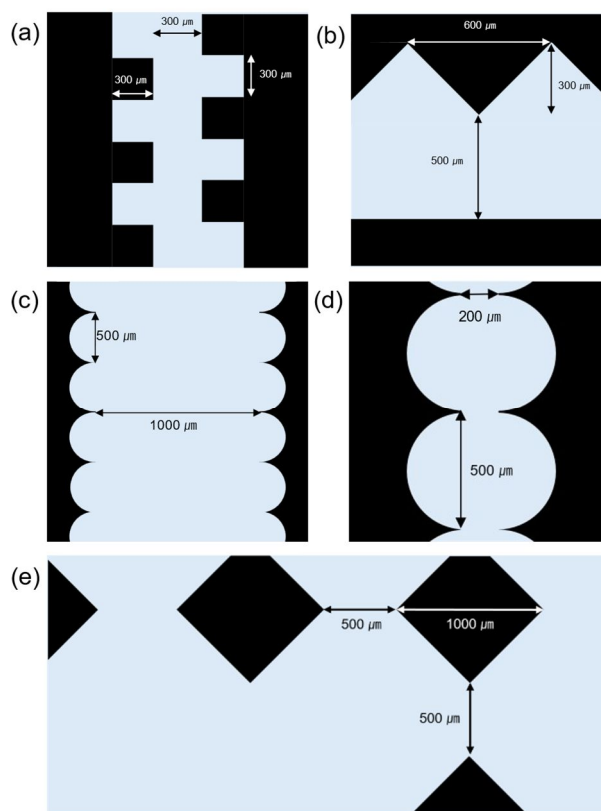


Figure S3. Schematic illustrations of the patterned electrode designs with detailed dimensions. The black regions indicate patterned gold electrodes, while the light blue regions represent masked substrate areas left uncoated during deposition. (a) A staggered castellated electrode. (b) A triangular-tipped electrode with an opposing flat edge. (c) Opposing sharp-tipped electrodes with the large gap. (d) Opposing sharp-tipped electrodes with the small gap. (e) An array of square island-shaped electrodes.

Evaluation of dielectrophoretic trapping and separation efficiency

Figure S4 presents the frequency-dependent dielectrophoretic trapping and separation performance of 2 μm and 10 μm polystyrene (PS) particles. For quantitative analysis, time-lapse image sequences were processed using ImageJ (National Institutes of Health, Bethesda, MD, USA). Specific regions of interest (ROIs) corresponding to pDEP and nDEP regions were defined using the ROI manager, and the ‘multi-measure’ function was employed to record intensity changes across frames. It should be noted that this analysis primarily reflects the projected areal coverage within the ROIs. Consequently, calculated efficiencies may appear lower than actual values if particles are highly concentrated or stacked in 3D within localized trapping regions (e.g., high-field regions for pDEP or low-field regions for nDEP), rather than spreading laterally. Under a 100 kHz electric field, 2 μm PS particles are gradually trapped in pDEP regions, showing a steady increase in trapping efficiency until equilibrium (**Fig. S4a**). In contrast, under a 1 MHz electric field, the same 2 μm PS particles exhibit nDEP behavior, where initially scattered particles are rapidly concentrated into low-field regions, causing a rise in trapping efficiency followed by saturation (**Fig. S4b**). In a mixture of 2 μm and 10 μm PS particles under a 100 kHz field, 2 μm PS particles exhibit pDEP while 10 μm PS particles show nDEP behavior, thereby enabling their effective spatial separation into distinct high- and low-field regions (**Fig. S4c**). These results demonstrate that the DEP response is highly dependent on particle size and frequency, confirming the feasibility of selective particle manipulation under controlled AC electric fields.

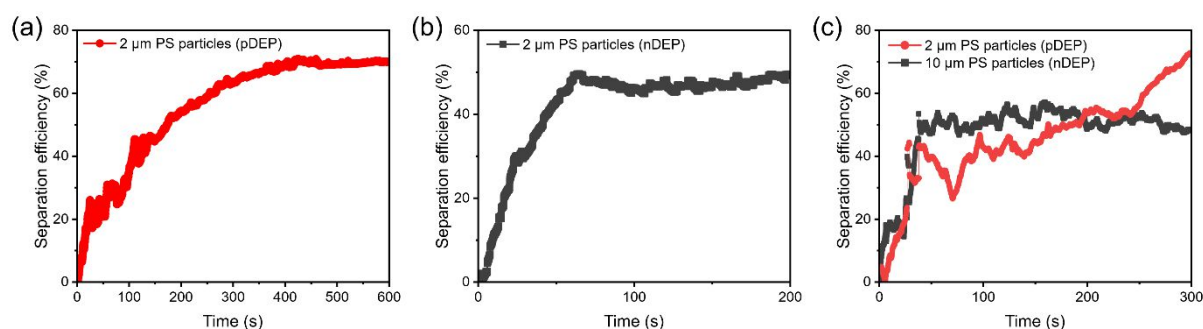


Figure S4. Time evolution of dielectrophoretic trapping and separation efficiency for polystyrene (PS) particles. (a) Trapping efficiency of 2 μm PS particles exhibiting pDEP behavior under a 100 kHz electric field. (b) Trapping efficiency of 2 μm PS particles exhibiting nDEP behavior under a 1 MHz electric field. (c) Separation efficiency of a mixture of 2 μm (pDEP) and 10 μm (nDEP) PS particles.

Effect of electrode spacing on dielectrophoretic assembly connectivity

To investigate the dependence of dielectrophoretic assembly on electrode spacing, we designed opposing sharp-tipped electrode pairs with gaps ranging from 200 μm to 1000 μm in 200 μm increments (**Fig. S5a**). This setup allowed for a systematic analysis of how electric-field confinement affects particle assembly as separation increases (**Fig. S5b**).

At relatively short gaps of 200 μm (**Fig. S5b,i**) and 400 μm (**Fig. S5b,ii**), the spacing was smaller than the lateral distance to adjacent patterns (500 μm ; **Fig. S3d**), producing strong localized fields that favored direct chain formation across all gaps. In these cases, continuous gold microwires bridged the electrodes, indicating that field confinement dominated the assembly process.

As the interelectrode distance increased beyond the lateral tip spacing (500 μm ; **Fig. S3c**) to 600 μm (**Fig. S5b,iii**) and 800 μm (**Fig. S5b,iv**), the field gradient across the gaps weakened relative to the local field of forming chains. Consequently, subsequently assembling particles were preferentially attracted laterally toward pre-existing chains rather than initiating new bridges. This competitive merging process primarily reduced the number of connected chains. As the gap further increased to 1000 μm (**Fig. S5b,v**), this lateral attraction became strong enough to induce Y-shaped side-branching.

The average number of connected gold chains (**Fig. S5c**) supports this trend: short gaps (200 and 400 μm) yielded consistent bridging, whereas larger gaps (600 and 800 μm) showed a pronounced reduction in chain formation, accompanied by side branching at 1000 μm . Thus, the assembly process transitions from uniform one-dimensional wire formation to competitive, branched network growth as electrode spacing increases.

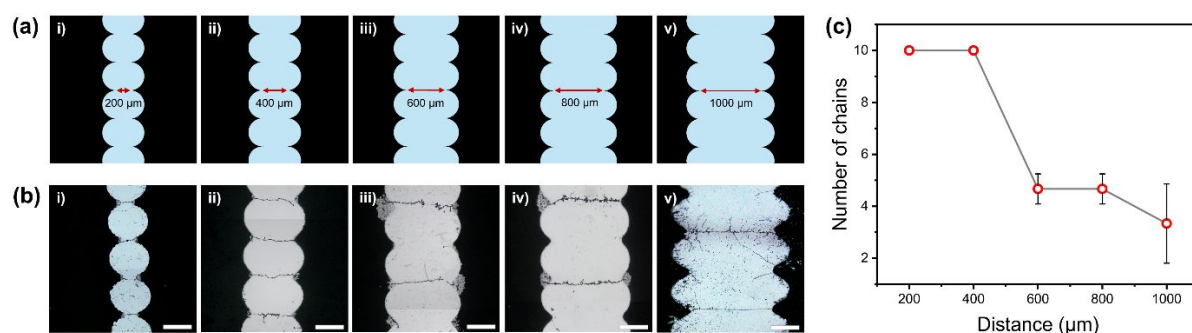


Figure S5. Dependence of gold chain formation on the sharp-tipped electrode gap distance. (a) Schematic illustration of the electrode configurations with varying inter-electrode distances. (b) Optical microscope images of gold chains formed between electrodes under applied electric fields ranging from 3.5 to 8 V peak-to-peak at 100 kHz. As the electrode gap increases, the number of assembled chains decreases and branching structures become more pronounced. Scale bars: 400 μm . (c) Average number of connected chains at each electrode spacing ($N=3$). Out of 10 possible connections, short gaps (200 and 400 μm) exhibit complete chain formation (10/10; not all shown in the images), whereas larger gaps (600, 800, and 1000 μm) result in a significant decrease in the number of connected chains.

References

- 1 S. O'Halloran, A. Pandit, A. Heise and A. Kellett, *Adv. Sci.*, 2023, **10**, 1–18.
- 2 M. Keough, J. F. McLeod, T. Salomons, P. Hillen, Y. Pei, G. Gibson, K. McEleney, R. Oleschuk and Z. She, *RSC Adv.*, 2021, **11**, 21600–21606.
- 3 F. Modica, V. Basile and I. Fassi, *Preprints.org*, 2024, DOI:10.20944/preprints202403.0520.v1.
- 4 A. I. Bunea, N. del Castillo Iniesta, A. Droumpali, A. E. Wetzel, E. Engay and R. Taboryski, *Micro*, 2021, **1**, 164–180.
- 5 M. D. Nelson, P. A. Tresco, C. C. Yost and B. K. Gale, *Lab Chip*, 2024, **24**, 4632–4638.
- 6 C. Zhang, K. Khoshmanesh, F. J. Tovar-Lopez, A. Mitchell, W. Wlodarski and K. Klantar-Zadeh, *Microfluid. Nanofluidics*, 2009, **7**, 633–645.
- 7 Q. Chen and Y. J. Yuan, *RSC Adv.*, 2019, **9**, 4963–4981.